ACCOUNTS
of chemical research

Signatures of Nonequilibrium Solvation Dynamics on Multidimensional Spectra

PORSCHA L. MCROBBIE,[†] GABRIEL HANNA,[†] QIANG SHI,[‡] AND EITAN GEVA[†,*]

[†]Department of Chemistry, University of Michigan, Ann Arbor, Michigan 48109-1055,
[‡]Beijing National Laboratory for Molecular Sciences, State Key Laboratory for Structural Chemistry of Unstable and Stable Species, Institute of Chemistry, Chinese Academy of Sciences (CAS), Zhongguancun, Beijing 100190, P. R. China

RECEIVED ON JANUARY 12, 2009

CONSPECTUS

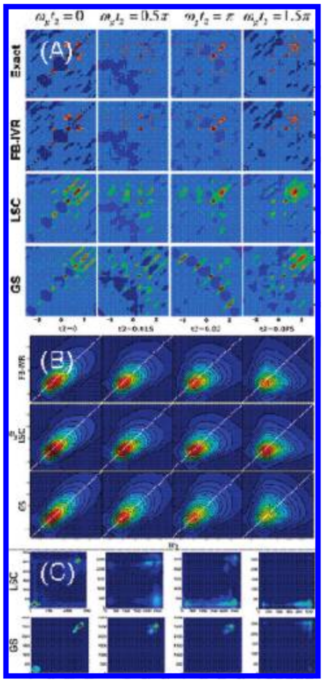

Multidimensional electronic and vibrational spectroscopies have established themselves over the last decade as uniquely detailed probes of intramolecular structure and dynamics. However, these spectroscopies can also provide powerful tools for probing solute−solvent interactions and the solvation dynamics that they give rise to. To this end, it should be noted that multidimensional spectra can be expressed in terms of optical response functions that differ with respect to the chromophore's quantum state during the various time intervals separating light−matter interactions. The dynamics of the photoinactive degrees of freedom during those time intervals (that is, between pulses) is dictated by potential energy surfaces that depend on the corresponding state of the chromophore. One therefore expects the system to hop between potential surfaces in a manner dictated by the optical response functions. Thus, the corresponding spectra should reflect the system's dynamics during the resulting sequence of nonequilibrium solvation processes. However, the interpretation of multidimensional spectra is often based on the assumption that they reflect the equilibrium dynamics of the photoinactive degrees of freedom on the potential surface that corresponds to the chromophore's ground state.

In this Account, we present a systematic analysis of the signature of nonequilibrium solvation dynamics on multidimensional spectra and the ability of various computational methods to capture it. The analysis is performed in the context of the following three model systems: (A) a two-state chromophore with shifted harmonic potential surfaces that differ in frequency, (B) a two-state atomic chromophore in an atomic liquid, and (C) the hydrogen stretch of a moderately strong hydrogen-bonded complex in a dipolar liquid. The following computational methods are employed and compared: (1) exact quantum dynamics (model A only), (2) the semiclassical forward−backward initial value representation (FB-IVR) method (models A and B only), (3) the linearized semiclassical (LSC) method (all three models), and (4) the standard ground-state equilibrium dynamics approach (all three models).

The results demonstrate how multidimensional spectra can be used to probe nonequilibrium solvation dynamics in real time and with an unprecedented level of detail. We also show that, unlike the standard method, the LSC and FB-IVR methods can accurately capture the signature of solvation dynamics on the spectra. Our results also suggest that LSC and FB-IVR yield similar results in the presence of rapid dephasing, which is typical in complex condensed-phase systems. This observation gives credence to the use of the LSC method for modeling spectra in complex systems for which an exact or even FB-IVR-based calculation is prohibitively expensive.

Published on the Web 06/24/2009 www.pubs.acs.org/acr
10.1021/ar800280s CCC: $71.50

I. Introduction

Multidimensional electronic and vibrational spectroscopies have long been recognized as extremely powerful and uniquely detailed probes of the structure and dynamics of molecular systems and have been used to elucidate a variety of processes on a wide range of time scales, including population and phase relaxation, energy and coherence transfer, intramolecular vibrational dynamics, chemical exchange, and conformational dynamics.[1−4] It is also widely accepted that molecularly detailed and dynamically accurate models are necessary in order to take full advantage of these capabilities. However, accomplishing this objective requires overcoming a number of nontrivial theoretical and computational challenges, including the design of spectroscopically accurate force fields, the choice of a proper dynamical treatment, and the development of schemes for calculating spectral signals that are both feasible and self-consistent.

Multidimensional spectra are often given in terms of optical response functions (ORFs).[1] However, a quantum-mechanically exact calculation of these ORFs is not feasible in most cases of practical interest. Mixed quantum−classical methods, which are based on treating a small subset of the degrees of freedom (DOF) quantum-mechanically while the rest are treated in a classical-like manner, therefore represent an attractive approach. However, taking the classical limit of the ORFs with respect to a subset of DOF in a direct manner is known to lead to expressions that are not unique.[5−11] In practice, the working expressions for the ORFs are often obtained in an ad-hoc manner to allow for their calculation from *equilibrium* classical molecular dynamics simulations of the photoinactive DOF on the potential surface that corresponds to the ground state of the photoactive DOF (see section IID). In what follows, we will refer to this approach as the *ground state* (GS) method.

A more rigorous approach toward calculating ORFs is based on linearizing the path-integral forward−backward action associated with the photoinactive DOF with respect to the difference between the forward and backward paths (see section IIC).[9,11−16] Within this approach, one calculates the ORFs by propagating the classical DOF *forward* in time along a classical trajectory that hops between potential surfaces corresponding to various quantum states of the chromophore, as dictated by the Liouville pathway associated with each ORF.[11] In what follows, we will refer to this approach as the *linearized semiclassical* (LSC) method.

Another rigorous approach to computing ORFs is based on replacing the product of quantum propagators that appears in the expressions for the ORFs by the corresponding forward−backward semiclassical propagators.[9,11,12,17−22] In what follows, we will refer to this approach as the *forward−backward initial-value representation* (FB-IVR) method (see section IIB).

In this Account, we present the results of a systematic investigation of the signature of nonequilibrium solvation dynamics on multidimensional spectra in three model systems: (A) a two-state chromophore with shifted harmonic potential surfaces that differ in frequency, which serves as a benchmark for which the quantum-mechanically exact ORFs can be computed; (B) an atomistically detailed model of an atomic chromophore in a two-dimensional atomic liquid, for which it is feasible to compute the ORFs via FB-IVR; and (C) a molecularly detailed model of a hydrogen-bonded (H-bonded) complex in a dipolar liquid, for which LSC and GS are the only feasible options. The ability of the LSC and FB-IVR approaches to accurately capture nonequilibrium solvation is first established in the context of model A. The ability of LSC to yield results similar to those obtained via FB-IVR, in the presence of rapid dephasing, is then established in the context of model B. Finally, model C is used to demonstrate the information-rich signature of nonequilibrium solvation on multidimensional spectra of a relatively complex molecular system within the framework of the LSC method.

The remainder of this Account is organized as follows: In section II, we present the exact quantum-mechanical expressions for the multidimensional spectra (section IIA) and formulate the corresponding FB-IVR (section IIB), LSC (section IIC), and GS (section IID) approximations. The results for the various model systems are presented and discussed in sections III, IV, and V. Conclusions and outlook are provided in section VI.

II. Theory

A. Third-Order Optical Response Functions and Multidimensional Spectra. For the sake of simplicity, we restrict ourselves to the case of a two-state system with the following generic field-free Hamiltonian:

$$\hat{H} = |g\rangle \hat{H}_g \langle g| + |e\rangle \hat{H}_e \langle e| \tag{1}$$

Here, $|g\rangle$ and $|e\rangle$ are the adiabatic ground and excited states of the chromophore, $\hat{H}_{g/e} = T(\hat{\mathbf{P}}) + V_{g/e}(\hat{\mathbf{Q}})$ are the corresponding adiabatic Hamiltonians, $T(\hat{\mathbf{P}})$ and $V_{g/e}(\hat{\mathbf{Q}})$ are the kinetic and potential energy, respectively, and $\hat{\mathbf{Q}} = (\hat{Q}_1,\ldots, \hat{Q}_N)$ and $\hat{\mathbf{P}} = (\hat{P}_1,\ldots, \hat{P}_N)$ are the coordinates and momenta of the photoinactive DOF.

The measurement of multidimensional spectra involves three sequential laser pulses with wave vectors $\mathbf{k}_a$, $\mathbf{k}_b$, and $\mathbf{k}_c$;

t_1 is the time delay between pulses a and b, and t_2 is the time delay between pulses b and c. These three pulses create a third-order polarization in the sample, which gives rise to a signal field that is heterodyne detected at a time interval t_3 after pulse c, in the background-free directions $\mathbf{k}_{\mathrm{r}} = -\mathbf{k}_{\mathrm{a}} + \mathbf{k}_{\mathrm{b}} + \mathbf{k}_{\mathrm{c}}$ and $\mathbf{k}_{\mathrm{nr}} = \mathbf{k}_{\mathrm{a}} - \mathbf{k}_{\mathrm{b}} + \mathbf{k}_{\mathrm{c}}$, corresponding to the *rephasing* and *nonrephasing* signals, respectively.[2] Assuming that the pulses are weak and impulsive, the nonrephasing and rephasing signals are given by[1]

$$R_{\mathrm{nr}}(t_3, t_2, t_1) = R_1(t_3, t_2, t_1) + R_4(t_3, t_2, t_1) \tag{2}$$

and

$$R_{\mathrm{r}}(t_3, t_2, t_1) = R_2(t_3, t_2, t_1) + R_3(t_3, t_2, t_1) \tag{3}$$

where the ORFs $\{R_1,R_2,R_3,R_4\}$ are explicitly given by[1]

$$R_1(t_3, t_2, t_1) = \mathrm{Tr}[\hat{\rho}_g\, \mathrm{e}^{i\hat{H}_g t_1/\hbar}\, \hat{\mu}_{ge}\, \mathrm{e}^{i\hat{H}_e t_2/\hbar}\, \hat{\mu}_{eg}\, \mathrm{e}^{i\hat{H}_g t_3/\hbar}\, \hat{\mu}_{ge}\, \mathrm{e}^{-i\hat{H}_e(t_1+t_2+t_3)/\hbar}\, \hat{\mu}_{eg}] \tag{4}$$

$$R_2(t_3, t_2, t_1) = \mathrm{Tr}[\hat{\rho}_g\, \mathrm{e}^{i\hat{H}_e(t_1+t_2)/\hbar}\, \hat{\mu}_{eg}\, \mathrm{e}^{i\hat{H}_g t_3/\hbar}\, \hat{\mu}_{ge}\, \mathrm{e}^{-i\hat{H}_e(t_2+t_3)/\hbar}\, \hat{\mu}_{eg}\, \mathrm{e}^{-i\hat{H}_g t_1/\hbar}\, \hat{\mu}_{ge}] \tag{5}$$

$$R_3(t_3, t_2, t_1) = \mathrm{Tr}[\hat{\rho}_g\, \mathrm{e}^{i\hat{H}_e t_1/\hbar}\, \hat{\mu}_{eg}\, \mathrm{e}^{i\hat{H}_g(t_2+t_3)/\hbar}\, \hat{\mu}_{ge}\, \mathrm{e}^{-i\hat{H}_e t_3/\hbar}\, \hat{\mu}_{eg}\, \mathrm{e}^{-i\hat{H}_g(t_1+t_2)/\hbar}\, \hat{\mu}_{ge}] \tag{6}$$

$$R_4(t_3, t_2, t_1) = \mathrm{Tr}[\hat{\rho}_g\, \mathrm{e}^{i\hat{H}_g(t_1+t_2+t_3)/\hbar}\, \hat{\mu}_{ge}\, \mathrm{e}^{-i\hat{H}_e t_3/\hbar}\, \hat{\mu}_{eg}\, \mathrm{e}^{-i\hat{H}_g t_2/\hbar}\, \hat{\mu}_{ge}\, \mathrm{e}^{-i\hat{H}_e t_1/\hbar}\, \hat{\mu}_{eg}] \tag{7}$$

Here, the trace is over the photoinactive DOF, $\hat{\mu}_{ge} = \mu_{ge}(\hat{\mathbf{Q}}) = \mu_{eg}^{\dagger}(\hat{\mathbf{Q}})$ is the transition dipole moment (an operator in the Hilbert space of the photoinactive DOF), and $\hat{\rho}_g = \mathrm{e}^{-\beta\hat{H}_g}/\mathrm{Tr}[\mathrm{e}^{-\beta\hat{H}_g}]$ is the equilibrium ground-state density operator, with $\beta = 1/(k_{\mathrm{B}}T)$. Finally, measurements of third-order optical response are often conveniently reported in terms of a two-dimensional (2D) spectrum, which is defined by

$$I(\omega_3, t_2, \omega_1) \equiv \mathrm{Re}\int_0^{\infty} \mathrm{d}t_1 \int_0^{\infty} \mathrm{d}t_3 \{\mathrm{e}^{i(\omega_1 t_1 + \omega_3 t_3)}\, R_{\mathrm{nr}}(t_3, t_2, t_1) + \mathrm{e}^{i(-\omega_1 t_1 + \omega_3 t_3)}\, R_{\mathrm{r}}(t_3, t_2, t_1)\} \tag{8}$$

B. The FB-IVR Approximation. Within the simplest implementation of the FB-IVR approximation, one starts by assuming that $\mu_{ge}(\hat{\mathbf{Q}}) \rightarrow \mu_{ge}$ is constant (the Condon approximation), followed by replacing the remaining *overall forward−backward time propagators* in eqs 4−7 by the corresponding semiclassical Herman−Kluk propagators[12,23] so that[9,11,17−20]

$$R_i^{\text{FB-IVR}}(t_3, t_2, t_1) = |\mu_{ge}|^4 \frac{1}{(2\pi\hbar)^N} \int \mathrm{d}\mathbf{Q}_0\, \mathrm{d}\mathbf{P}_0\, D(\mathbf{P}_0, \mathbf{Q}_0) \langle g_{\mathbf{P}_0\mathbf{Q}_0}|\hat{\rho}_g|g_{\mathbf{P}_f\mathbf{Q}_f}\rangle\, \mathrm{e}^{i/\hbar S_i} \tag{9}$$

Here, $|g_{\mathbf{P}_t\mathbf{Q}_t}\rangle$ is a coherent state,

$$\langle \mathbf{Q}|g_{\mathbf{P}_t\mathbf{Q}_t}\rangle = \left(\frac{1}{\pi}\right)^{N/4} (\det \gamma)^{1/4} \exp\left(-\frac{1}{2}(\mathbf{Q} - \mathbf{Q}_t)^T \cdot \gamma \cdot (\mathbf{Q} - \mathbf{Q}_t) + \frac{i}{\hbar}\mathbf{P}_t \cdot (\mathbf{Q} - \mathbf{Q}_t)\right) \tag{10}$$

where γ is a constant positive definite matrix, which is assumed to be diagonal in what follows; $D(\mathbf{P}_0,\mathbf{Q}_0)$ is the Herman−Kluk prefactor and $\{S_i\}$ are the forward−backward actions (the explicit expressions can be found in ref 11). These actions are calculated along classical trajectories, which are propagated forward in time from time 0 to $t_1 + t_2 + t_3$ and then backward in time from time $t_1 + t_2 + t_3$ to 0. It should also be noted that throughout these forward−backward trajectories, the system hops between the ground and excited potential surfaces according to eqs 4−7.

C. The LSC Approximation. The LSC approximation is based on writing the ORFs in a path integral form and linearizing the path-integral forward−backward action with respect to the difference between the forward and backward paths.[9,11,13−16] It leads to expressions for the ORFs of the following form:

$$\begin{aligned} R_j^{\text{LSC}}(t_3, t_2, t_1) &= \frac{1}{(2\pi\hbar)^N} \int \mathrm{d}\mathbf{Q}_0\, \mathrm{d}\mathbf{P}_0\, \rho_{g,\mathrm{W}}(\mathbf{Q}_0, \mathbf{P}_0)\mu_{ge}(\mathbf{Q}_0)\, \times \\ &\quad \mu_{ge}(\mathbf{Q}_{t_1})\mu_{ge}(\mathbf{Q}_{t_1+t_2})\mu_{ge}(\mathbf{Q}_{t_1+t_2+t_3})\, \mathrm{e}^{-i\int_0^{t_1} \mathrm{d}\tau U(\mathbf{Q}_\tau)/\hbar}\, \mathrm{e}^{\mp i\int_{t_1+t_2}^{t_1+t_2+t_3} \mathrm{d}\tau U(\mathbf{Q}_\tau)/\hbar} \equiv \\ &\quad \langle \mu_{ge}(\mathbf{Q}_0)\mu_{ge}(\mathbf{Q}_{t_1})\mu_{ge}(\mathbf{Q}_{t_1+t_2})\mu_{ge}(\mathbf{Q}_{t_1+t_2+t_3})\, \mathrm{e}^{-i\int_0^{t_1} \mathrm{d}\tau U(\mathbf{Q}_\tau)/\hbar}\, \mathrm{e}^{\mp i\int_{t_1+t_2}^{t_1+t_2+t_3} \mathrm{d}\tau U(\mathbf{Q}_\tau)/\hbar} \rangle_{g,\mathrm{W}} \end{aligned} \tag{11}$$

Here, + and − correspond to rephasing ORFs (R_2,R_3) and nonrephasing ORFs (R_1,R_4), respectively, $\rho_{g,\mathrm{W}}(\mathbf{Q},\mathbf{P})$ is the Wigner transform of $\hat{\rho}_g$,

$$\rho_{g,\mathrm{W}}(\mathbf{Q}, \mathbf{P}) = \int \mathrm{d}\Delta\, \mathrm{e}^{-i\mathbf{P}\cdot\Delta/\hbar} \left\langle \mathbf{Q} + \frac{\Delta}{2} \middle| \hat{\rho}_g \middle| \mathbf{Q} - \frac{\Delta}{2} \right\rangle \tag{12}$$

$\mu_{ge}(\mathbf{Q})$ is the transition dipole moment at the classical bath configuration $\mathbf{Q}$ (which can be assumed to be real without loss of generality), and $U(\mathbf{Q}_\tau) = V_e(\mathbf{Q}_\tau) - V_g(\mathbf{Q}_\tau)$. Importantly, $\{\mathbf{Q}_\tau\}$ are classical trajectories whose initial states are sampled from $\rho_{g,\mathrm{W}}(\mathbf{Q}_0,\mathbf{P}_0)$ and that hop between potential surfaces as they are propagated forward in time from time 0 to $t_1 + t_2 + t_3$. More specifically, the propagation takes place on the average potential surface, $V_{ge} = (V_g + V_e)/2$, during (0, t_1) and (t_1

$+ t_2, t_1 + t_2 + t_3$), and on either the excited-state potential surface, V_e (in the case of R_1 and R_2), or the ground-state potential surface, V_g (in the case of R_3 and R_4), during (t_1, $t_1 + t_2$). Finally, it should be noted that in deriving eq 11, we have neglected the quantum nature of the transition dipole moment operator, $\mu_{ge}(\hat{\mathbf{Q}})$, which is expected to be a reasonable approximation at ambient conditions.

D. The GS Approximation. The GS approximation can be obtained with the help of the following identity:[1]

$$\exp[-i\hat{H}_j t/\hbar] = \exp[-i\hat{H}_{\text{ref}} t/\hbar]\ \exp_+[-i\int_0^t \mathrm{d}t'\ \hat{U}_j(t')/\hbar] \tag{13}$$

Here, $\exp_+$ corresponds to a positively time-ordered exponential, $\hat{H}_{\text{ref}}$ is an *arbitrarily chosen reference Hamiltonian* and

$$\hat{U}_j(t) = \exp[i\hat{H}_{\text{ref}} t/\hbar]\ (\hat{H}_j - \hat{H}_{\text{ref}})\ \exp[-i\hat{H}_{\text{ref}} t/\hbar] \tag{14}$$

The GS approximation relies on the ad-hoc choice of the reference Hamiltonian as the ground-state Hamiltonian: $\hat{H}_{\text{ref}} = \hat{H}_g$. For example, applying the identity in eq 13, with the choice of $\hat{H}_{\text{ref}} = \hat{H}_g$, to the ORF $R_1(t_1, t_2, t_3)$ in eq 4 yields

$$R_1(t_3, t_2, t_1) = \mathrm{Tr}[\hat{\rho}_g \hat{\mu}_{ge}(t_1)\ \exp_-[i\int_{t_1}^{t_1+t_2} \mathrm{d}t'\hat{U}(t')/\hbar]\hat{\mu}_{eg}(t_1 + t_2)\hat{\mu}_{ge}(t_1 + t_2 + t_3)\ \exp_-[-i\int_0^{t_1+t_2+t_3} \mathrm{d}t'\hat{U}(t')/\hbar]\hat{\mu}_{eg}(0)] \tag{15}$$

where $\exp_-$ corresponds to a negatively time-ordered exponential, $\hat{U}(t) = \exp[i\hat{H}_g t/\hbar][\hat{V}_e - \hat{V}_g]\ \exp[-i\hat{H}_g t/\hbar]$ and $\hat{\mu}_{ge}(t) = \exp[i\hat{H}_g t/\hbar]\ \hat{\mu}_{ge}\ \exp[-i\hat{H}_g t/\hbar]$. Taking the "classical limit" of $R_1(t_1,t_2,t_3)$ corresponds to replacing the trace by a phase-space average, $\hat{\rho}_g$ by the corresponding ground-state equilibrium phase-space density $\rho_{g,\text{cl}}(\mathbf{Q}_0,\mathbf{P}_0)$, $\hat{A}(t)$ by its classical analogue $A[\mathbf{Q}_t]$, where $\mathbf{Q}_t$ is a classical trajectory on the ground-state potential surface, and the time-ordered exponentials by regular exponentials. The resulting GS approximation for $R_1(t_1,t_2,t_3)$ is then given by

$$\begin{aligned} R_1^{\text{GS}}(t_3, t_2, t_1) = \int \mathrm{d}\mathbf{Q}_0\ \mathrm{d}\mathbf{P}_0\ \rho_{g,\text{cl}}(\mathbf{Q}_0, \mathbf{P}_0)\mu_{ge}(\mathbf{Q}_0)\ \times \\ \mu_{ge}(\mathbf{Q}_{t_1})\mu_{ge}(\mathbf{Q}_{t_1+t_2})\mu_{ge}(\mathbf{Q}_{t_1+t_2+t_3})\ \mathrm{e}^{-i\int_0^{t_1} \mathrm{d}\tau U(\mathbf{Q}_\tau)/\hbar}\ \mathrm{e}^{-i\int_{t_1+t_2}^{t_1+t_2+t_3} \mathrm{d}\tau U(\mathbf{Q}_\tau)/\hbar} \equiv \\ \langle \mu_{ge}(\mathbf{Q}_0)\mu_{ge}(\mathbf{Q}_{t_1})\mu_{ge}(\mathbf{Q}_{t_1+t_2})\mu_{ge}(\mathbf{Q}_{t_1+t_2+t_3})\ \mathrm{e}^{-i\int_0^{t_1} \mathrm{d}\tau U(\mathbf{Q}_\tau)/\hbar}\ \mathrm{e}^{-i\int_{t_1+t_2}^{t_1+t_2+t_3} \mathrm{d}\tau U(\mathbf{Q}_\tau)/\hbar} \rangle_{g,\text{cl}} \end{aligned} \tag{16}$$

Similar approximations can be obtained for the other ORFs, yielding $R_4^{\text{GS}}(t_3,t_2,t_1) = R_1^{\text{GS}}(t_3,t_2,t_1)$ and

$$\begin{aligned} R_2^{\text{GS}}(t_3, t_2, t_1) = R_3^{\text{GS}}(t_3, t_2, t_1) = \\ \langle \mu_{ge}(\mathbf{Q}_0)\mu_{ge}(\mathbf{Q}_{t_1})\mu_{ge}(\mathbf{Q}_{t_1+t_2})\mu_{ge}(\mathbf{Q}_{t_1+t_2+t_3}) \\ \mathrm{e}^{-i\int_0^{t_1} \mathrm{d}\tau U(\mathbf{Q}_\tau)/\hbar}\ \mathrm{e}^{i\int_{t_1+t_2}^{t_1+t_2+t_3} \mathrm{d}\tau U(\mathbf{Q}_\tau)/\hbar} \rangle_{g,\text{cl}} \end{aligned} \tag{17}$$

Although the GS approximation in eqs 16 and 17 is similar in form to the LSC approximation, eq 11, it differs from it in two important respects, namely:

- The classical trajectories in the case of GS take place exclusively on the ground-state potential surface.
- The sampling of the initial state in the case of GS is based on the classical ground-state Boltzmann probability density rather than the Wigner transform of the corresponding quantum-mechanical density operator.

It should also be noted that unlike the FB-IVR and LSC approximations, which reflect *nonequilibrium* dynamics on multiple potential surfaces, the GS approximation reflects *equilibrium* dynamics on the ground-state potential surface.

III. A Two-State Chromophore with Shifted Different-Frequency Harmonic Potential Surfaces

The first model that we will consider contains a single photoinactive mode and assumes that the potential energy surface as a function of this mode's displacement is harmonic in both the ground and excited states:

$$V_g(\hat{Q}) = \frac{1}{2}{\omega_g}^2\hat{Q}^2; \quad V_e(\hat{Q}) = \hbar\omega_{eg} + \frac{1}{2}{\omega_e}^2(\hat{Q} + Q_0)^2 \tag{18}$$

Here, $\hat{Q}$ is the mass-weighted displacement of the photoinactive mode, ω_g and ω_e are its harmonic frequencies in the ground and excited states, respectively, Q_0 is the shift of the excited-state surface relative to the ground-state surface, and ω_{eg} is the minimum to minimum transition frequency between the ground state and excited state.

Importantly, the exact quantum-mechanical ORFs can be obtained for this model, in terms of the vibronic transition frequencies and corresponding Franck–Condon coefficients.[1] We also assume that ω_{eg} is a stochastic quantity satisfying Gaussian statistics in the limit of motional narrowing, so that $R_j(t_1, t_2, t_3) = \exp[-\Gamma(t_1 + t_3)]\bar{R}_j(t_1,t_2,t_3)$, where Γ is the electronic dephasing rate constant and $\{\bar{R}_j(t_1, t_2, t_3)\}$ correspond to the undamped parts of the ORFs.

It should be noted that the special case where $\omega_e = \omega_g$, which corresponds to the one-dimensional version of the popular Brownian oscillator model,[1] does not lend itself as a benchmark for the problem at hand. This is because the dynamics on the ground and excited states are governed by

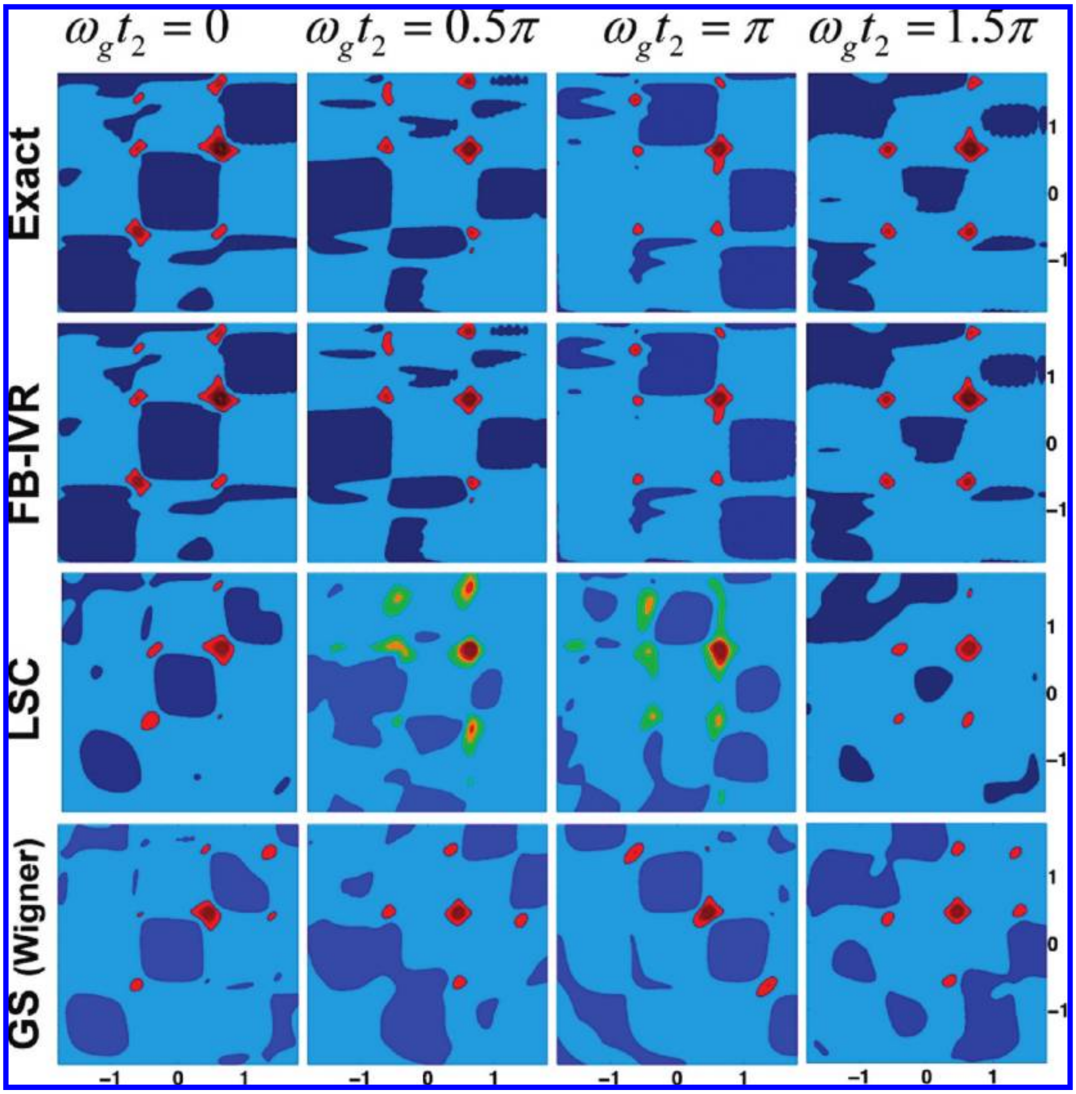

FIGURE 1. Two-dimensional spectra for a two-state chromophore with shifted different-frequency harmonic potential surfaces at $T = 0.2\hbar\omega_g/k_B$. The *x* and *y* axes correspond to ω_1/ω_g and ω_3/ω_g, respectively. The spectra are shown for the specified values of the waiting time, t_2. Shown are the exact results (top panels) and the results obtained via FB-IVR (second panels from top), LSC (third panels from top), and GS (bottom panels).

potential surfaces that have the exact same shape. Indeed, within the Condon approximation, a second-order cumulant expansion based on the quantum-mechanical equilibrium ground-state frequency−frequency correlation function is known to provide the exact result in this case.[1] Furthermore, the LSC and FB-IVR approximations coincide with the exact ORFs when $\omega_e = \omega_g$. Thus, choosing a model system with $\omega_e \neq \omega_g$ is necessary for it to be a meaningful benchmark in the context of the present study.

Exact 2D spectra for this model system, as well as the corresponding FB-IVR, LSC, and GS approximations, are shown in Figures 1 and 2 at $T = 0.2\hbar\omega_g/k_B$ (low temperature) and $T = 5.0\hbar\omega_g/k_B$ (high temperature), respectively. The results in these figures were obtained for the following values of the parameters: $\omega_e/\omega_g = 1.25$, $Q_0 = (\hbar/\omega_g)^{1/2}$, $\Gamma = \omega_g/(4\pi)$ and $\gamma = \omega_g/\hbar$. We have also assumed that the frequency origin is set at $(\omega_1, \omega_3) = (\langle\omega_{eg}\rangle, \langle\omega_{eg}\rangle)$, where $\langle\omega_{eg}\rangle$ is the average of the stochastic variable $\omega_{eg}(t)$. Since sampling the initial state based on the classical Boltzmann distribution clearly represents a poor approximation at low temperatures, we have used the Wigner distribution in order to generate the GS results in this case (see bottom panels in Figure 1). We have also shifted the ω_1 and ω_3 frequency axes by $\omega_g/2$ in the case of GS in order to account for zero point energy effects.

As expected, the quantum-mechanically exact 2D spectra consist of peaks at the various vibronic frequencies (see top panels in Figures 1 and 2). The widths of these peaks are determined by Γ, which was purposely chosen to be relatively narrow in this case, and their intensities are determined by the thermal weight of the initial state and the corresponding prod-

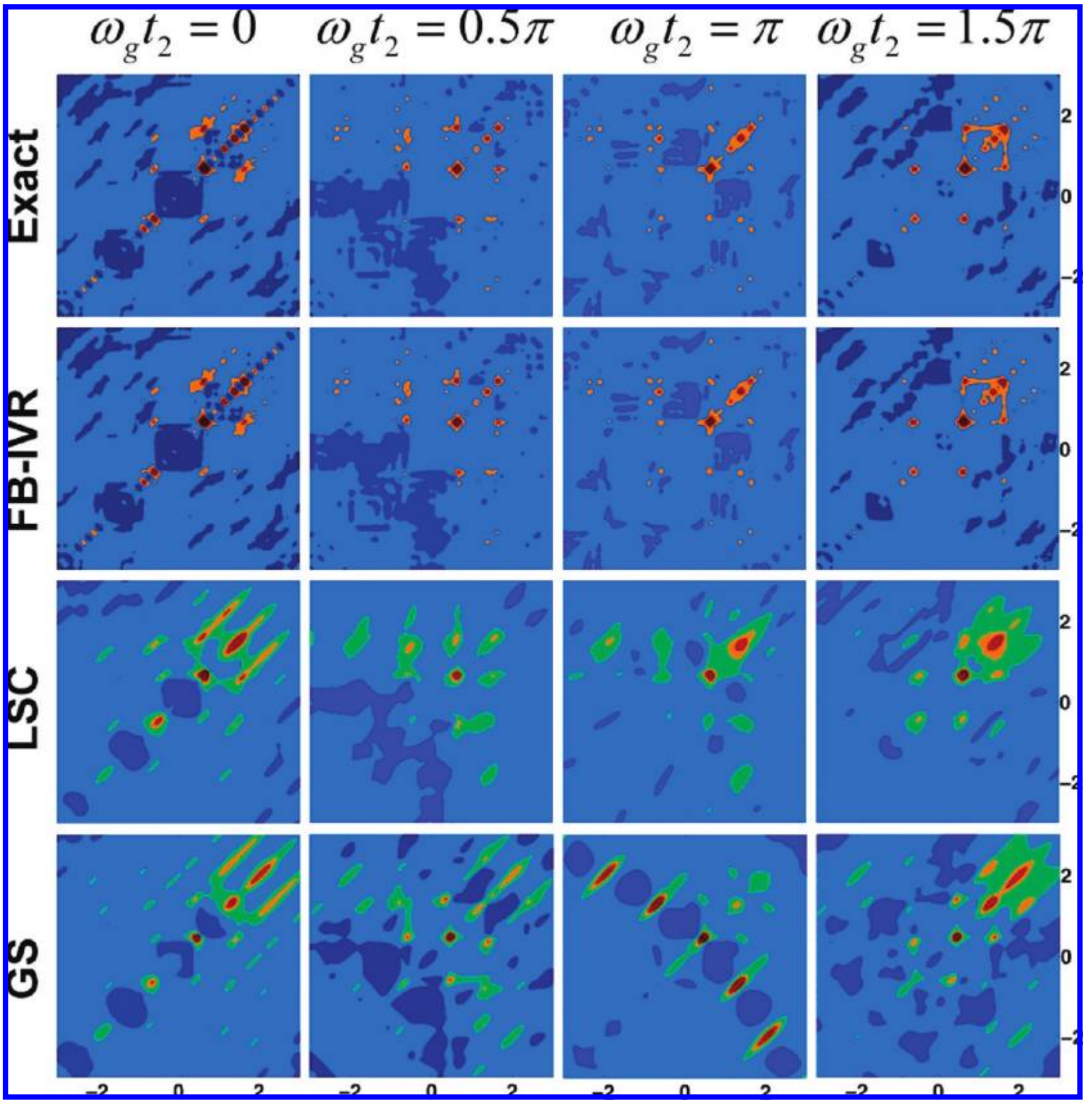

FIGURE 2. Two-dimensional spectra for a two-state chromophore with shifted different-frequency harmonic potential surfaces at $T = 5.0\hbar\omega_g/k_B$. The x and y axes correspond to ω_1/ω_g and ω_3/ω_g, respectively. The spectra are shown for the specified values of the waiting time, t_2. Shown are the exact results (top panels) and the results obtained via FB-IVR (second panels from top), LSC (third panels from top), and GS (bottom panels).

ucts of Franck−Condon coefficients. The number of peaks is seen to increase with temperature, which reflects the larger number of initially populated ground vibronic states.

The 2D spectra obtained via FB-IVR are seen to be in excellent agreement with the exact results, at both high and low temperatures (see second from the top panels in Figures 1 and 2). However, it should be noted that the fact that the coherent state width parameter, γ, was chosen to be constant implies that FB-IVR is not exact for the system considered here. More specifically, by assuming that γ is constant, FB-IVR neglects the fact that what is a coherent state on one surface corresponds to a squeezed state on the other surface. However, the relatively small difference between ω_g and ω_e implies that the changes in the width will be rather small and, as a result, have almost no effect on the spectra.

We next turn to the 2D spectra obtained via LSC (see third from the top panels in Figures 1 and 2). The locations and relative intensities of the peaks that constitute the 2D spectra are reproduced rather well at all values of t_2. However, the peaks are seen to be broader, which suggests that the LSC approximation gives rise to nonphysical dephasing, which adds to the physically meaningful electronic dephasing, thereby overestimating the line widths. This observation is consistent with the previously reported inability of the LSC approximation to capture long-lived coherences because of overdamping, which can be attributed to the fact that it is based on purely classical all-forward dynamics and therefore lacks the ability to account for interference effects.[12,16,24] Thus, the LSC approach would be particularly suitable for modeling 2D spectra in molecular systems at ambient conditions where the ultrafast physical dephasing is expected to dominate any nonphysical dephasing.

Finally, we consider the spectra obtained via GS (see bottom panels in Figures 1 and 2). Although the agreement between the exact spectra and those obtained via GS at $t_2 = 0$ is reasonable, significant deviations between the spectra emerge at longer t_2. It should be noted that unlike the case of LSC, the deviations in the case of GS are qualitative and correspond to different peak locations and relative intensities. This is hardly surprising in light of the fact that the spectra obtained via GS are insensitive to excited state dynamics. Indeed, a breakdown of the spectra into contributions from the various ORFs show that the deviations mostly come from R_1 and R_2, which correspond to Liouville pathways where the dynamics during t_2 is governed by the excited-state potential surface. It should also be noted that the deviations between GS and the exact results do not diminish with increasing temperature, which testifies to the fact that GS does not represent a rigorous classical limit of the spectra.

IV. A Two-State Atomic Chromophore Solvated in a Two-Dimensional Atomic Liquid

The next model system that we consider consists of a single atomic two-state chromophore in a 2D atomic liquid. The details of the model were described in refs 9 and 11 and will only be briefly outlined below for the sake of completeness. A 2D simulation cell with periodic boundary conditions was employed, which contained 25 atoms. The potential energy for the ground and excited states was assumed to be pairwise additive with pair potentials of the Lennard-Jones (LJ) type. One of the atoms was designated as the chromophore and the LJ parameter σ in the chromophore−solvent interaction pair potential in the ground state was assumed to be different from that in the excited state ($\sigma_e = 1.06\sigma_g$). The Wigner transform $\rho_{g,W}(\mathbf{Q},\mathbf{P})$ was approximated via the local harmonic approximation.[9] The results reported below are based on simulations performed at the following temperature and density: $T^* = k_B T/\varepsilon = 1.07$, and $\rho^* = \rho\sigma^2 = 0.7$, in terms of reduced LJ units. The remaining results are also reported in terms of reduced LJ units (for comparison, the real time unit is 2.16 ps in the case of liquid argon).

The recently reported calculated 2D spectra for this system (within the Condon approximation) via the FB-IVR, LSC, and GS approximations[11] are reproduced in Figure 3. The main observation is that while the 2D spectra in the case of GS are symmetrical with respect to reflection about the diagonal ($\omega_1 = \omega_3$), they become increasingly asymmetrical with increasing t_2 when calculated via the LSC and FB-IVR approximations. The deviations from diagonal symmetry can be traced back to contributions from R_1 and R_2, which involve nonequilibrium solvation dynamics on the excited-state potential surface during t_2. The signature of these nonequilibrium solvation processes is captured within the LSC and FB-IVR methods but missed by the GS method. We also note the quantitative similarity between the spectra obtained via LSC and FB-IVR, which suggests that the line broadening observed in the 2D spectra calculated via LSC reflects genuine physical dephasing.

V. A Moderately Strong H-Bonded Complex in a Dipolar Liquid

The last model system that we will consider consists of a moderately strong H-bonded complex, AHB, in a dipolar liquid.[25−28] Within this model, it is assumed that the proton moves along a one-dimensional axis connecting the donor and acceptor. The donor, A, and acceptor, B, are modeled as single particles and parametrized to represent phenol and trimethylamine, respectively. The intramolecular potential surface as a function of the A−B and A−H distances is as in refs 26−28 with the equilibrium A−B distance set to 2.7 Å. The charges on A and B are assumed to be explicitly dependent on the position of the proton. The intramolecular potential surface has a double-well profile as a function of the proton displacement, thereby giving rise to tautomeric equilibrium between covalent and ionic forms: $\mathrm{AH{-}B} \rightleftharpoons \mathrm{A^{-}{-}H^{+}B}$. The solvent is assumed to consist of a liquid of methyl-chloride molecules, which are modeled as rigid dipolar diatomic molecules. The complex−solvent and solvent−solvent interactions are modeled in terms of site−site LJ and Coulomb interactions, and the corresponding force field parameters are as in refs 26−28.The photoactive DOF is taken to be the high-frequency H-stretch. The remaining DOF are assumed to follow the high-frequency H-stretch *adiabatically*, so the vibrational energy levels and wave functions are obtained by diagonalizing the adiabatic protonic Hamiltonian on-the-fly.[26−28] Molecular dynamics simulations were performed with a single AHB complex and 255 methyl-chloride molecules in a cubic simula-

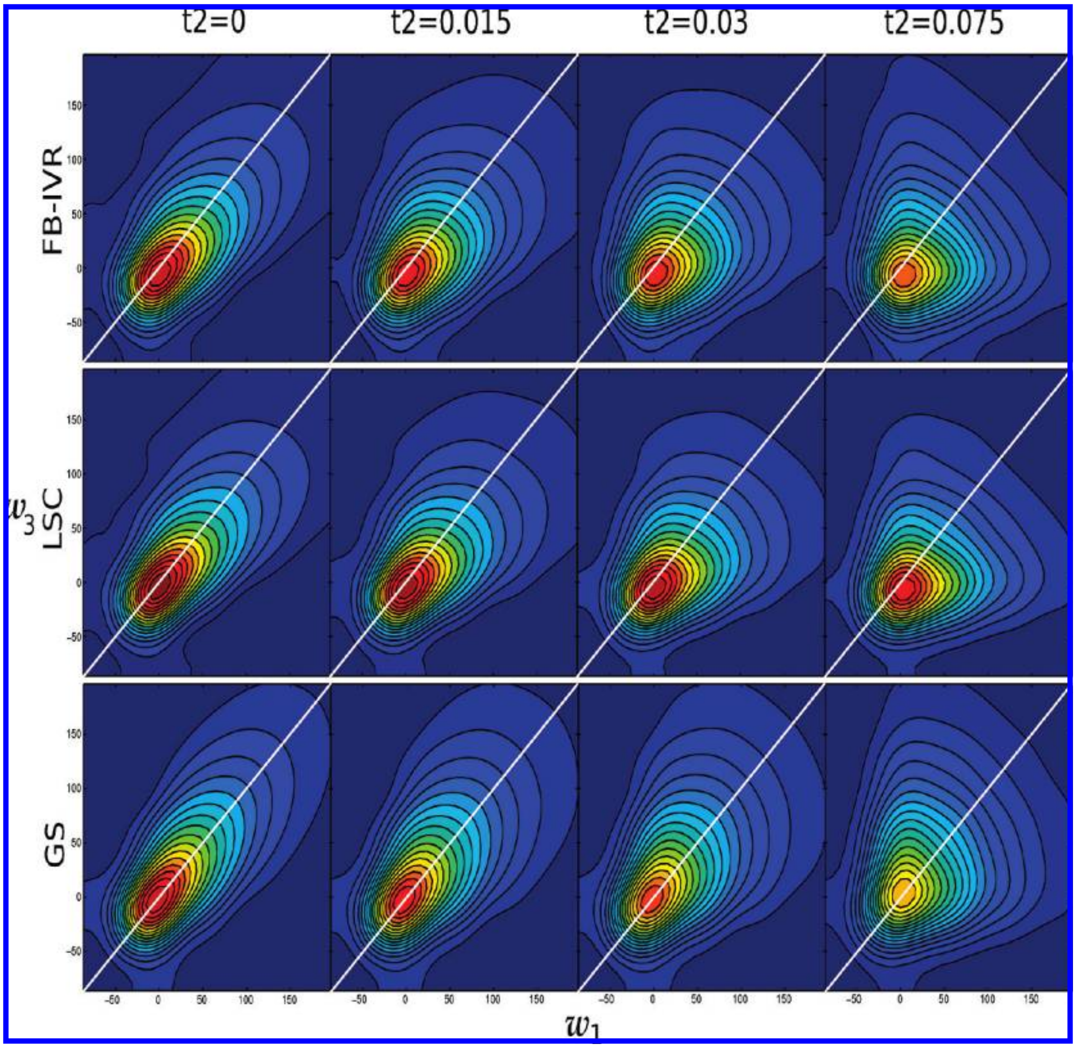

FIGURE 3. Two-dimensional spectra for a two-state atomic chromophore in 2D liquid solution at the specified values of the waiting time t_2 as calculated within the FB-IVR (upper panel), LSC (middle panel), and GS (bottom panel) approximations. The results are given in terms of reduced LJ units. Reproduced from ref 11.

tion box with periodic boundary conditions at a temperature and density of 250 K and 0.012 Å^{-3}, respectively.

The ground (*g*) and first-excited (*e*) free energy surfaces (FESs) are shown as a function of the solvent polarization (as defined in refs 26, 29, and 30) in the top panel of Figure 4. The ground-state FES has a double-well form, which reflects coexistence between the ionic and covalent tautomers (equilibrium composition: 65% ionic and 35% covalent; proton transfer rate constant: 0.16 ps^{-1}).[30] In contrast, the excited FES has the shape of a single well whose minimum is centered in the vicinity of the ground-state transition state between the ionic and covalent tautomers. It is important to note that the ionic/covalent tautomers and transition state correspond to stable and unstable solvent configurations, respectively, only on the ground-state surface. In contrast, the solvent configurations corresponding to the transition state and the ionic/covalent tautomers are stable and unstable, respectively, on the excited-state potential. Thus, one can expect significant solvation effects in this system.

The distribution of the transition frequency, ω_{eg}, as obtained from equilibrium simulations on the ground and excited potential surfaces, is shown in the middle panel of Figure 4. In the lower panel of Figure 4, we show the same distributions of ω_{eg} but this time weighted by the square of the transition dipole moment, $|\mu_{eg}(\mathbf{Q})|^2$. The rather dramatic difference between the distributions in the middle and lower panels of Figure 4 can be traced back to a breakdown of the Condon approximation due to the strong dependence of the transition dipole moment on **Q**, which makes the transition dipole moments negligibly small within the intermediate frequency range ~(500,1500) cm^{-1}.[27] It should also be noted that the high-frequency band on the lower panel of Figure 4 consists of contributions from the ionic (~2500 cm^{-1}) and covalent (~2250 cm^{-1}) tautomers, while the low frequency band

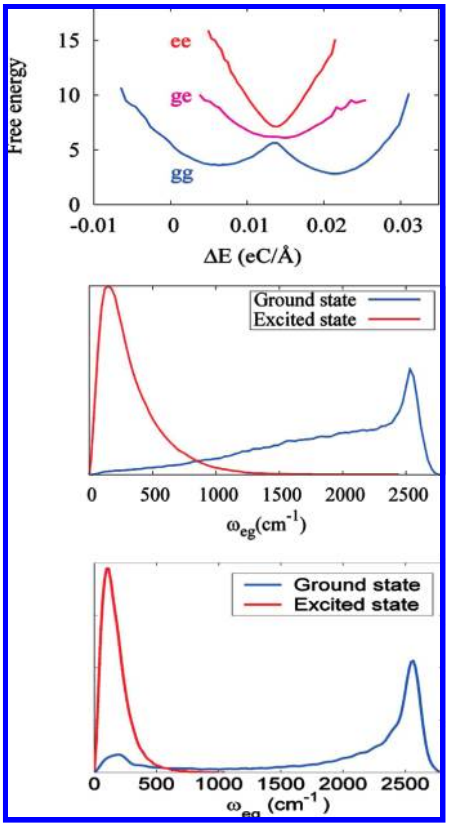

FIGURE 4. Top panel, the ground (blue, gg), excited (red, ee), and average (magenta, ge) free energy surfaces of the H stretch in a H-bonded complex dissolved in a dipolar liquid as a function of the solvent polarization; middle panel, the distribution of the transition frequency, ω_{eg}, as obtained from equilibrium simulations on the ground (blue) and excited (red) potential surfaces; bottom panel, the same distributions of the transition frequency, ω_{eg}, weighted by the square of the transition dipole moment, $|\mu_{eg}(\mathbf{Q})|^2$.

($\sim$200 cm^{-1}) arises from configurations in the vicinity of the transition state.[27]

The 2D infrared (IR) spectra for this system as obtained via the LSC and GS approximations are shown in the top and bottom panels of Figure 5, respectively, for the specified values of t_2.[27,31] We did not attempt to apply the FB-IVR method to this model system because of the high computational cost of such a calculation and the expectation that spectra calculated via FB-IVR and LSC will be similar in the presence of ultrafast dephasing (see Figure 3). We have also substituted the Wigner distribution in the case of LSC by the corresponding classical ground state equilibrium probability density, which is expected to be an excellent approximation near ambient conditions.

The main spectral features in the 2D spectra obtained via GS and LSC at $t_2 = 0$ are similar. More specifically, one observes three diagonal peaks that correspond to the ionic ($\sim$2500 cm^{-1}), covalent ($\sim$2250 cm^{-1}), and transition-state ($\sim$200 cm^{-1}) subpopulations. The similarity of the spectra at $t_2 = 0$ can be traced back to the fact that solvation on the average potential is limited by the short dephasing time during t_1 and t_3 ($\sim$150 fs). Nevertheless, the effect of nonequilibrium solvation on the average potential is discernible even at $t_2 = 0$ and manifests itself by the increased intensity of the transition-state peak at the expense of the ionic and covalent peaks in the LSC-based 2D spectrum. This is because solvation on the average surface during t_1 and t_3 drives the solvent away from configurations that correspond to the ionic and covalent species and toward configurations that correspond to the transition state, thereby enhancing contributions from the latter at the expense of the former.

The deviations between the spectra obtained via LSC and GS become significantly larger with increasing t_2. Within LSC, starting at equilibrium on the ground-state potential, the first pulse is most likely to excite the system within the ionic, covalent, and transition-state bands. As discussed above, the state of the system changes relatively little during the short time it spends on the average potential between the first and second pulse (t_1). The second pulse then either returns the system to the ground-state potential (R_3 and R_4) or places it on the excited state potential (R_1 and R_2). Thus, in the case of R_3 and R_4, the ensuing nonequilibrium solvation during t_2 drives the system away from the transition-state configuration and toward the ionic and covalent configurations. However, the opposite is true in the case of R_1 and R_2, where the ensuing nonequilibrium solvation during t_2 drives the system away from the ionic and covalent configurations and toward the transition-state configurations. Since the intermediate spectral range between the high-frequency ionic/covalent band and low-frequency transition-state band is photoinactive, solvation actually manifests itself by a loss of signal at intermediate times (see $t_2 = 125$ fs of the upper panel of Figure 4). However, the signal reappears when the system reaches either the ionic/covalent bands, in the case of R_3 and R_4, or the transition state, in the case of R_1 and R_2.

Upon complete solvation ($t_2 \approx 500$ fs[26]), one expects the dynamics during t_1 to become uncorrelated with that during t_3. Thus, within LSC, the 2D spectrum is asymptotically proportional to $I_{\mathrm{A}}^{\mathrm{LSC}}(\omega_1)I_{\mathrm{E}}^{\mathrm{LSC}}(\omega_3) + I_{\mathrm{A}}^{\mathrm{LSC}}(\omega_1)I_{\mathrm{A}}^{\mathrm{LSC}}(\omega_3)$, where $I_{\mathrm{A}}^{\mathrm{LSC}}(\omega)$ and $I_{\mathrm{E}}^{\mathrm{LSC}}(\omega)$ correspond to the Fourier–Laplace transforms of $\langle \mu_{ge}[\mathbf{Q}_0]\mu_{ge}[\mathbf{Q}_t]\ \mathrm{e}^{-i\int_0^t \mathrm{d}\tau U(\mathbf{Q}_\tau)/\hbar}\rangle_{g,\mathrm{cl}}$ and $\langle \mu_{ge}[\mathbf{Q}_0]\mu_{ge}[\mathbf{Q}_t]\ \mathrm{e}^{-i\int_0^t \mathrm{d}\tau U(\mathbf{Q}_\tau)/\hbar}\rangle_{e,\mathrm{cl}}$, which are closely related to the absorption and emission spectra, respectively, as calculated within LSC (i.e., $\langle \cdots \rangle_{g,\mathrm{cl}}$ and $\langle \cdots \rangle_{e,\mathrm{cl}}$ indicate initial sampling that corresponds to equilibrium on the ground or excited potential surfaces, respectively, and the dynamics of $\mathbf{Q}_\tau$ during t_1 and t_3 takes place on the average potential). It should also be noted that the contribu-

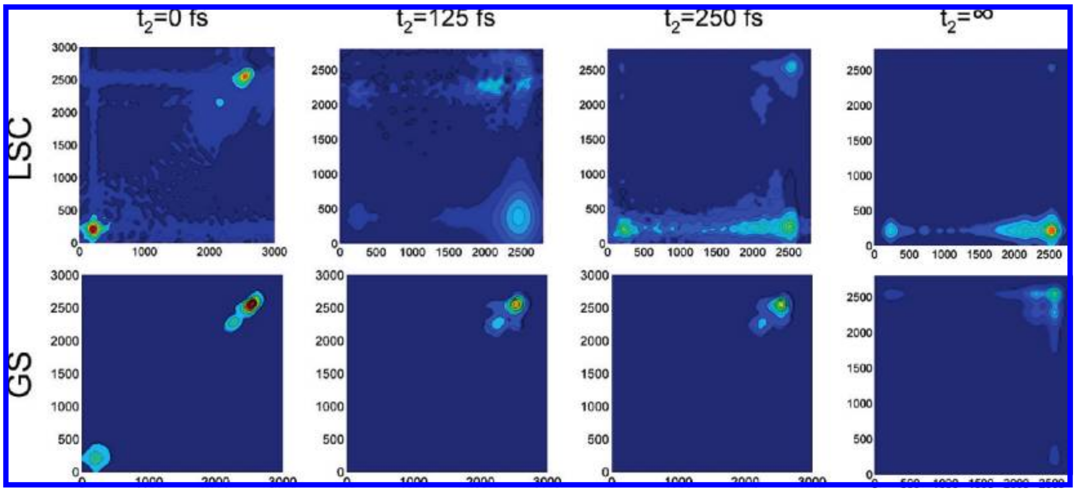

FIGURE 5. Two-dimensional IR spectra of the H stretch in a H-bonded complex dissolved in a dipolar liquid at the specified values of the waiting time, t_2, as calculated within LSC (top panels) and GS (bottom panels).

tions from R_1 and R_2, which give rise to a spectral feature of the form $I_A^{LSC}(\omega_1)I_E^{LSC}(\omega_3)$, dominates the spectrum.

In contrast, within GS, $R_2 = R_3$, $R_1 = R_4$, and the dynamics takes place exclusively on the ground-state potential surface. As a result, the diagonal transition-state peak starts out weaker at $t_2 = 0$ and vanishes at longer t_2 because the transition state corresponds to unstable solvent configurations on the ground-state potential surface. At even longer t_2, the dynamics during t_1 become uncorrelated with that during t_3, so the 2D spectrum becomes proportional to $I_A^{GS}(\omega_1)I_A^{GS}(\omega_3)$, where $I_A^{GS}(\omega)$ corresponds to the Fourier–Laplace transform of $\langle \mu_{ge}[\mathbf{Q}_0]\mu_{ge}[\mathbf{Q}_t] e^{-i\int_0^t d\tau U(\mathbf{Q}_\tau)/\hbar}\rangle_{g,\mathrm{cl}}$. Thus, the LSC and GS spectra are observed to approach fundamentally different limits at long t_2.

VI. Conclusions and Outlook

In this paper, we explored the ability of the FB-IVR, LSC, and GS methods to describe the signature of nonequilibrium solvation dynamics on multidimensional spectra. The analysis was performed on three model systems that range from a benchmark corresponding to a two-state chromophore with shifted harmonic potential surfaces that differ in frequency to a more realistic model of a moderately strong H-bonded complex in a polar liquid.

Our results demonstrate the many ways in which 2D spectra can be used in order to probe nonequilibrium solvation dynamics in real time with an unprecedented level of detail. More specifically, we have found that nonequilibrium solvation processes can impact 2D spectra in a *qualitative* manner by breaking their symmetry, shifting spectral features, intensifying some spectral features at the expense of others, and giving rise to completely new spectral features that are absent from the spectra obtained via the GS method. The observation of many of these signatures relies on the unique ability of 2D spectroscopy to correlate between transition frequencies at different times and opens the door to new ways of using 2D spectroscopy to directly probe the many important chemical events, such as the formation of the transition state, which occur far from equilibrium on the ground-state surface.

We have also found that unlike the commonly used GS method, the LSC and FB-IVR methods can capture the signature of solvation dynamics on the spectra in an accurate manner. Our results suggest that 2D spectra calculated via the LSC method are similar to those calculated via the FB-IVR method in the presence of ultrafast dephasing, which is typically the case in complex condensed phase systems. This observation gives credence to the use of the LSC method for modeling 2D spectra in complex systems for which an exact quantum-mechanical, or even the approximate but rather expensive FB-IVR method, may not be feasible.

E.G. is grateful to the National Science Foundation (Grant No. CHE-0809506) and the Petroleum Research Fund for financial support. Q.S. gratefully acknowledges the supports from the National Natural Science Foundation of China (Grant Nos. 20733006 and 20873157) and from the Chinese Academy of Sciences.

BIOGRAPHICAL INFORMATION

Porscha L. McRobbie received her B.S. in Physics and a B.A. in Chemistry from Seattle University in 2002. She is currently a Ph.D. candidate at the University of Michigan, Ann Arbor.

Gabriel Hanna received his B.Sc. in Chemistry at Laurentian University in 2001 and his Ph.D. in Chemistry at the University of Toronto in 2006. He is currently a Postdoctoral Fellow at the University of Michigan, Ann Arbor.

Qiang Shi received his B.S. in Mathematics and Physics in 1995 and Ph.D. in Physical Chemistry in 2000 from the University of Science and Technology of China. He is currently a Chemistry Professor at the Institute of Chemistry, Chinese Academy of Sciences.

Eitan Geva received his B.Sc. in Chemistry in 1989 and Ph.D. in Theoretical Chemistry in 1996 from the Hebrew University of Jerusalem. He is currently a Chemistry Professor at the University of Michigan, Ann Arbor.

FOOTNOTES

*To whom correspondence should be addressed. E-mail: eitan@umich.edu.

REFERENCES

1 Mukamel, S. *Principles of Nonlinear Optical Spectroscopy*; Oxford: New York, 1995.

2 Khalil, M.; Demirodoven, N.; Tokmakoff, A. Coherent 2D IR spectroscopy: Molecular structure and dynamics in solution. *J. Phys. Chem. A* **2003**, *107*, 5258–5279.

3 Jonas, D. M. Two-dimensional femtosecond spectroscopy. *Annu. Rev. Phys. Chem.* **2003**, *54*, 425–463.

4 Cho, M. Coherent two-dimensional optical spectroscopy. *Chem. Rev.* **2008**, *108*, 1331–1418.

5 Mukamel, S. On the semiclassical calculation of molecular absorption and fluorescence spectra. *J. Chem. Phys.* **1982**, *77*, 173–183.

6 Shemetulskis, N. E.; Loring, R. F. Semiclassical theory of the photon echo: Application to polar fluids. *J. Chem. Phys.* **1992**, *97*, 1217–1226.

7 Saven, J. G.; Skinner, J. L. A molecular theory of the line shape: Inhomogeneous and homogeneous electronic spectra of dilute chromophores in nonpolar fluids. *J. Chem. Phys.* **1993**, *99* (6), 4391–4402.

8 Stephens, M. D.; Saven, J. G.; Skinner, J. L. Molecular theory of electronic spectroscopy in nonpolar fluids: Ultrafast solvation dynamics and absorption and emission line shapes. *J. Chem. Phys.* **1997**, *106*, 2129–2144.

9 Shi, Q.; Geva, E. A comparison between different semiclassical approximations for optical response functions in nonpolar liquid solutions. *J. Chem. Phys.* **2005**, *122*, 064506.

10 Ka, B. J.; Geva, E. A nonperturbative calculation of nonlinear spectroscopic signals in liquid solution. *J. Chem. Phys.* **2006**, *125*, 214501.

11 Shi, Q.; Geva, E. A comparison between different semiclassical approximations for optical response functions in nonpolar liquid solution II. the signature of excited state dynamics on two-dimensional spectra. *J. Chem. Phys.* **2008**, *129*, 124505.

12 Miller, W. H. Including quantum effects in the dynamics of complex (i.e. large) molecular systems. *J. Chem. Phys.* **2006**, *125*, 132305.

13 Shi, Q.; Geva, E. A relationship between semiclassical and centroid correlation functions. *J. Chem. Phys.* **2003**, *118*, 8173–8184.

14 Shi, Q.; Geva, E. A semiclassical theory of vibrational energy relaxation in the condensed phase. *J. Phys. Chem. A* **2003**, *107*, 9059–9069.

15 Shi, Q.; Geva, E. Vibrational energy relaxation in liquid oxygen from a semiclassical molecular dynamics simulation. *J. Phys. Chem. A* **2003**, *107*, 9070–9078.

16 Shi, Q.; Geva, E. Nonradiative electronic relaxation rate constants from approximations based on linearizing the path-integral forward-backward action. *J. Phys. Chem. A* **2004**, *108*, 6109–6116.

17 Sepúlveda, M. A.; Mukamel, S. Semiclassical theory of molecular nonlinear optical polarization. *J. Chem. Phys.* **1995**, *102*, 9327–9344.

18 Spencer, C. F.; Loring, R. F. Dephasing of a solvated two-level system: A semiclassical approach for parallel computing. *J. Chem. Phys.* **1996**, *105*, 6596–6606.

19 Kühn, O.; Makri, N. Forward—backward semiclassical calculation of spectral line shapes: I_2 in a rare gas cluster. *J. Phys. Chem. A* **1999**, *103*, 9487–9493.

20 Ovchinnikov, M.; Apkarian, V. A.; Voth, G. A. Semiclassical molecular dynamics computation of spontaneous light emission in the condensed phase: Resonance Raman spectra. *J. Chem. Phys.* **2001**, *184*, 7130–7143.

21 Thompson, K.; Makri, N. Influence functionals with semiclassical propagators in combined forward-backward time. *J. Chem. Phys.* **1999**, *110*, 1343–1353.

22 Sun, X.; Miller, W. H. Forward-backward initial value representation for semiclassical time correlation functions. *J. Chem. Phys.* **1999**, *110*, 6635–6644.

23 Herman, M. F.; Kluk, E. A semiclassical justification for the use of non-spreading wave packets in dynamics calculations. *Chem. Phys.* **1984**, *91*, 27–34.

24 Egorov, S. A.; Rabani, E.; Berne, B. J. Vibronic spectra in condensed matter: A comparison of exact quantum mechanical and various semiclassical treatments for harmonic baths. *J. Chem. Phys.* **1998**, *108*, 1407–1422.

25 Azzouz, H.; Borgis, D. A quantum molecular-dynamics study of proton-transfer reactions along asymmetrical H bonds in solution. *J. Chem. Phys.* **1993**, *98*, 7361–7374.

26 Hanna, G.; Geva, E. Vibrational energy relaxation of a hydrogen-bonded complex dissolved in a polar liquid via the mixed quantum-classical Liouville method. *J. Phys. Chem. B* **2008**, *112*, 4048–4058.

27 Hanna, G.; Geva, E. A computational study of the one and two dimensional infrared spectra of a vibrational mode strongly coupled to its environment: Beyond the cumulant and condon approximations. *J. Phys. Chem. B* **2008**, *112*, 12991–13004.

28 Hanna, G.; Geva, E. Isotope effects on the vibrational relaxation and multidimensional infrared spectra of the hydrogen stretch in a hydrogen-bonded complex dissolved in a polar liquid. *J. Phys. Chem. B* **2008**, *112*, 15793–15800.

29 Hanna, G.; Kapral, R. Quantum-classical Liouville dynamics of nonadiabatic proton transfer. *J. Chem. Phys.* **2005**, *122*, 244505.

30 Hanna, G.; Kapral, R. Quantum-classical Liouville dynamics of proton and deuteron transfer rates in a solvated hydrogen bonded complex. *J. Chem. Phys.* **2008**, *128*, 164520.

31 Hanna, G.; Geva, E. Multidimensional spectra via the mixed quantum-classical Liouville method: Signatures of nonequilibrium dynamics. *J. Phys. Chem. B*, in press.